Converter-Level Modeling and Coordinated Control of a Wind–Battery Powered Surface Water Heat Pump DC Microgrid: Case Study of Ouistreham, France

Joyce Assaf, Mamadou-Baïlo Camara, Damien Guilbert, Brayima Dakyo
Groupe de Recherche en Electrotechnique et Automatique du Havre
Université Le Havre Normandie
Le Havre, Normandie, France
e-mail: {joyce.assaf | camaram | damien.guilbert | brayima.dakyo}@univ-lehavre.fr

***Abstract*—This paper presents the design and validation of a DC microgrid integrating two parallel 30 kW Surface Water Heat Pumps (SWHPs), a 35 kW Wind Turbine (WT), and a 35 kWh Battery Energy Storage System (BESS). The subsystems are interconnected through a regulated 1000 V DC–bus and coordinated via a hierarchical control strategy. A detailed MATLAB/Simulink model is developed using measured wind speed data from the Le Cano Ouistreham, France pilot site and realistic thermal demand data from an operational aquathermal installation in Dijlemolens, Belgium. A refined Region-III power limitation strategy for the WT and cascaded voltage–current control loops for the BESS are implemented to ensure stable operation under fluctuating wind conditions and high thermal demand. Simulation results demonstrate tight DC–bus regulation, with a maximum voltage deviation below 0.62% and a Root Mean Square Error (RMSE) of 0.033%. Under peak thermal demand of 52.32 kW, coordinated WT–BESS power sharing maintains supply continuity without violating operational constraints. The proposed DC microgrid architecture provides a validated and scalable framework for renewable-powered aquathermal heating systems.**

Keywords-DC microgrid; Wind Turbine; Surface Water Heat Pump; Battery Energy Storage System; Energy Management Strategy.

I. Introduction

This journal paper extends our previous conference contribution presented at GREEN 2025 [1], where the preliminary DC microgrid architecture and initial simulation results were introduced. The present version significantly expands the modeling framework, refines the Wind Turbine (WT) Region-III control strategy, incorporates a cascaded dual-loop DC–bus voltage and battery current control strategy for the Battery Energy Storage System (BESS), and provides an extended system-level performance analysis under realistic pilot-site operating conditions.

Aquathermal Energy (AE) is the extraction, storage, and distribution of heat from water bodies, including surface water, wastewater, and groundwater. It is an emerging Renewable Energy Source (RES) with strong potential for heating and cooling applications. In AE systems using surface water, heat is extracted from the water body using a Surface Water Heat Pump (SWHP) via a heat exchanger, which then increases or decreases the temperature as needed for domestic hot water supply and other thermal energy applications [2]. AE systems reduce carbon emissions in the heating and cooling sector and decrease its reliance on imported energy [3].

According to the latest IRENA report, 87 million Heat Pumps (HPs) are projected to be installed in buildings, with wind and solar expected to contribute 91% of the total Renewable Energy (RE) capacity by 2050 [4]. When coupled with RESs, such as wind or Photovoltaics (PVs) to power their compressors, SWHPs offer a promising pathway to decarbonize the building sector [5]. In Europe, the deployment of WTs is spreading rapidly, with wind energy accounting for almost 39% of the total electricity generated from RESs in 2024 [6]. However, due to the intermittent nature of WTs, BESSs are integrated to effectively manage short-term fluctuations, while appropriate control strategies can significantly improve system reliability and efficiency [7].

Power electronics play an essential role in enabling the efficient integration of HPs with RESs. DC-links, incorporating AC–DC and DC–DC converters, allow for improved energy management, voltage regulation, and efficient power conversion across hybrid systems. Compared to traditional AC microgrids, DC-based systems offer lower conversion losses, improved energy management, and more straightforward control, particularly advantageous for hybrid configurations with large shares of DC loads or storage units [8].

In the literature, several studies have explored hybrid systems for HP applications [9]–[12]. Although these studies laid essential groundwork, they often overlooked power electronics integration, realistic thermal demand modeling, and dynamic power management between sources and loads. Few studies addressed power electronics control strategies and converter topologies for RE-powered HPs. For instance, in [13], the authors proposed an energy management strategy (EMS) for a microgrid that combines a PV, a BESS, and an air-source HP. The main goal of the study was to reduce the cost of the BESS by leveraging the thermal storage of the HP, incorporating a double fuzzy logic that coordinates power fluctuation stabilization between the BESS and the air-source HP. However, HP operation was mainly governed by RE availability and system efficiency, not by actual, time-varying thermal demand.

In [14], the authors presented a hybrid system that includes PV, WT, and BESS powering a DC-HP. However, the approach is limited as it only accounts for the electrical power consumption of the HP, with the thermal load profile being derived from thermodynamic equations without incorporating its actual dynamics. As a result, the control and performance of the system are not realistically reflective of actual HP operation, which is typically governed by unpredictable and varying thermal loads over time. Furthermore, in [15], the authors proposed an advanced control strategy based on the model predictive control combined with a fractional short-circuit current approach to optimize power extraction from the PV system interfaced with a SWHP. However, this study modeled the SWHP as a resistive load, so results were only analyzed on the PV–BESS side. Alternatively, in [16], the authors proposed a high-voltage-gain DC–DC converter to improve PV-HP coupling efficiency. Although their converter showed promising results in handling variable solar irradiance, the system also lacked realistic thermal modeling of the HP. Although their work offers valuable insights, it remains unclear whether the results are scalable to real-world scenarios.

This paper contributes to the growing body of research on HPs, particularly SWHPs, by presenting a realistic simulation conducted for an AE harvesting pilot site within the "Water-Warmth" project, funded by Interreg North Sea Region, in Le Cano Ouistreham, France. This pilot site is currently in the preparatory phase for constructing a SWHP system, making it an ideal case study to simulate and validate RE integration and control strategies under realistic site conditions. The proposed system employs a 35 kW WT and a 35 kWh BESS to power two identical 30 kW SWHPs operating in parallel, all connected via a DC–bus with realistic control architecture, using both measured wind speeds from Ouistreham pilot site and thermal load profile from an operational site in Belgium. The originality of this study lies in its comprehensive simulation of component interactions between fluctuating RE generation and dynamic thermal demand, and its validation of a coordinated control strategy that ensures voltage stability under realistic fluctuating wind and load conditions. The proposed model provides a more accurate reflection of operational conditions and offers a pathway toward scalable, site-adapted AE solutions.

Unlike previous works that neglect realistic thermal demand dynamics or simplified power electronics modeling, this study integrates full electromechanical and converter-level modeling under measured site data.

In summary, the novelty of this work lies in three main contributions: (i) the use of real measured climatic and thermal demand profiles, preserving realistic variability in wind speed and heating demand; (ii) the coordinated control of the WT and the BESS to guarantee DC–bus voltage stability under high-load and fluctuating wind conditions, including a refined Region-III wind power limitation strategy; and (iii) the implementation of a DC microgrid that minimizes energy conversion stages, thereby improving structural efficiency and controllability.

The main objective of this study is to design and validate, through MATLAB/Simulink under real-site operating conditions, an EMS that ensures stable, demand-driven operation of a hybrid WT–BESS–SWHP DC microgrid.

This paper is organized as follows. Section I briefly reviews the state of the art in RE-powered heating systems. Section II presents the DC microgrid configuration, including the WT, BESS, SWHP units, and associated power electronic converters. Section III details the control framework implemented on the WT and BESS DC–DC converters, including voltage regulation and power-limiting strategies. Section IV discusses the performance analysis conducted under realistic pilot-site operating conditions within the framework of the WaterWarmth project. Finally, Section V concludes the paper and outlines key findings.

II. DC Microgrid Configuration

The rated power of the WT (35 kW) and the energy capacity of the BESS (35 kWh) were selected to ensure supply continuity under worst-case operating scenarios, particularly during simultaneous high thermal demand and low wind availability. The objective of this study is not to optimize energy capacity sizing, but rather to validate the coordinated control strategy and DC microgrid stability under realistic operating conditions.

A. Wind Turbine

The system shown in Figure 1 is based on a variable-speed WT coupled with a Permanent Magnet Synchronous Generator (PMSG), which converts mechanical energy to electrical energy. The rotating rotor blades extract kinetic energy from the wind and transform it into shaft torque, which is then converted into electricity by the generator. To maximize the energy extracted from the varying wind speeds, the system relies on control strategies that regulate the WT's rotor speed and blade pitch angle. A detailed description of the control strategy adopted is provided in Section III.

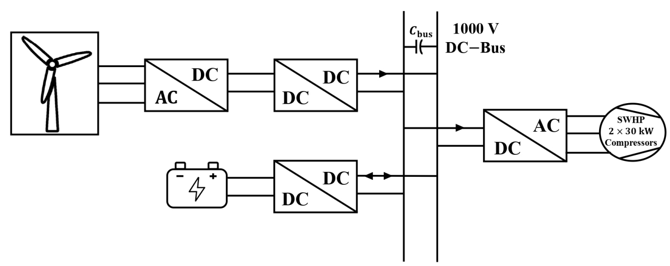

Figure 1. Overall configuration of the WT-BESS-SWHP system.

The wind speed data, illustrated in Figure 2, were collected for Le Cano Ouistreham, covering the period from March 7, 2024 at 11:00 AM to May 7, 2024 at 2:00 AM, with a sample time of one hour. The wind speed frequently drops below the 10.9 m/s nominal speed and occasionally falls near or below cut-in speed of the WT (3 m/s), reflecting the intermittent nature of wind energy. These fluctuations justify the need for both WT speed control to maximize energy capture under partial load conditions and the integration of a BESS to stabilize the system's power supply.

For computational feasibility, the original time-series datasets were temporally compressed and mapped onto a 1456 s simulation horizon while preserving their statistical variability and dynamic characteristics.

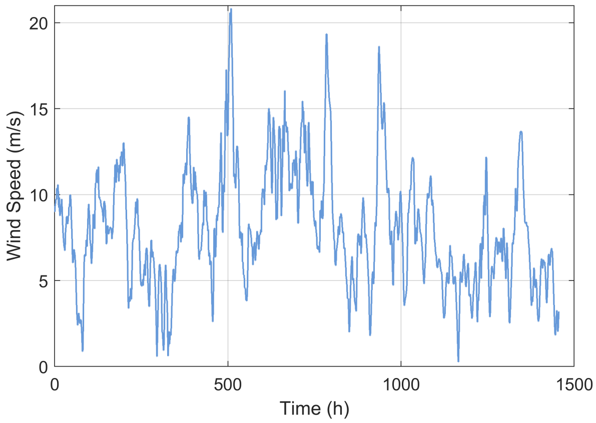

Figure 2. The wind speed profile in Le Cano Ouistreham, France.

1) Wind Turbine Aerodynamic Modeling: The mechanical power extracted from the wind by a horizontal-axis WT is expressed as:

$$P_{\text{aero}} = \frac{1}{2}\rho A C_p(\lambda,\beta) V_w^3 \tag{1}$$

where ρ is the air density (1.225 kg/m^3), $A = \pi R^2$ is the swept area of the rotor blades, C_p is the power coefficient, V_w is the wind speed, λ is the tip-speed ratio, and β is the blade pitch angle.

The tip-speed ratio is defined as:

$$\lambda = \frac{\omega_m R}{V_w} \tag{2}$$

where ω_m is the mechanical rotor speed and R is the turbine radius ($R = 5$ m).

The aerodynamic efficiency of the WT is characterized by the power coefficient $C_p(\lambda,\beta)$, which depends on the tip-speed ratio λ and the pitch angle β. In this study, a semi-empirical analytical approximation of the C_p surface is adopted to enable continuous simulation of aerodynamic behavior [17]:

$$\begin{aligned} C_p(\lambda,\beta) = {} & (0.5 - 0.00167(\beta-2))\sin\left(\frac{\pi(\lambda+0.1)}{18.5-0.3(\beta-2)}\right) \\ & - 0.00184(\lambda-3)(\beta-2) \end{aligned} \tag{3}$$

This formulation captures the nonlinear dependence of aerodynamic efficiency on both rotor speed and blade pitch angle. It enables realistic modeling of Region-II maximum power extraction and Region-III power limitation through pitch control.

For $\beta = 0°$, the function exhibits a maximum value $C_{p,\max} = 0.5276$ at the optimal tip-speed ratio $\lambda_{\text{opt}} = 9.7205$, which are the parameters used in this study.

In Region-II, the WT operates at the optimal tip-speed ratio λ_{opt} that maximizes the power coefficient:

$$C_p = C_{p,\max}, \quad \lambda = \lambda_{\text{opt}} \tag{4}$$

Under this condition, the wind speed can be expressed as:

$$V_w = \frac{\omega_m R}{\lambda_{\text{opt}}} \tag{5}$$

Substituting (5) into (1) yields:

$$P_{\text{opt}} = \frac{1}{2}\rho\pi R^2 C_{p,\max}\left(\frac{\omega_m R}{\lambda_{\text{opt}}}\right)^3 \tag{6}$$

Rearranging the terms leads to:

$$P_{\text{opt}} = \frac{1}{2}\rho\pi R^5 \frac{C_{p,\max}}{\lambda_{\text{opt}}^3}\omega_m^3 \tag{7}$$

For simplicity, the constant term is defined as:

$$K_{\text{opt}} = \frac{1}{2}\rho\pi R^5 \frac{C_{p,\max}}{\lambda_{\text{opt}}^3} \tag{8}$$

Thus, the reference power used for Maximum Power Point Tracking (MPPT) in Region-II becomes:

$$P_{\text{m,ref}} = K_{\text{opt}}\,\omega_m^3 \tag{9}$$

This formulation corresponds to the classical Optimal Torque Control (OTC) method used in variable-speed WTs. Unlike wind-speed-based MPPT strategies, this approach relies solely on the measured rotor speed, eliminating the need for wind sensors and improving robustness against measurement noise. It also provides a direct cubic relationship between rotor speed and extracted power, ensuring that the WT operates continuously at the maximum power coefficient under below-rated wind conditions.

In this study, the parameters used are $\rho = 1.225$ kg/m^3, $R = 5$ m, $C_{p,\max} = 0.5276$, and $\lambda_{\text{opt}} = 9.7205$, from which K_{opt} is computed according to Eq. (8).

2) Permanent Magnet Synchronous Generator Electromagnetic Modeling: The WT is coupled to a three-phase PMSG modeled in the rotor-oriented dq reference frame using the standard Park transformation. In this study, a surface-mounted (round rotor) machine with sinusoidal back electromotive force (back-EMF) is considered. Under this assumption, the d- and q-axis inductances are equal ($L_d = L_q = L_s$), and magnetic saliency effects are neglected.

The stator voltage equations in the synchronous dq reference frame are expressed as [18]:

$$\begin{aligned} v_d &= R_s i_d + L_s\frac{di_d}{dt} - \omega_e L_s i_q \\ v_q &= R_s i_q + L_s\frac{di_q}{dt} + \omega_e\left(L_s i_d + \lambda_m\right) \end{aligned} \tag{10}$$

where v_d and v_q are the stator voltages, i_d and i_q are the stator currents in the rotating dq frame, R_s is the stator phase resistance, L_s is the synchronous inductance, λ_m is the permanent magnet flux linkage, and ω_e is the electrical angular speed.

The electrical angular speed is related to the mechanical rotor speed by:

$$\omega_e = p\,\omega_m \tag{11}$$

where p denotes the number of pole pairs and ω_m is the mechanical angular speed of the rotor.

For a non-salient surface-mounted rotor ($L_d = L_q$), the electromagnetic torque expression simplifies to:

$$T_e = \frac{3}{2} p \lambda_m i_q \tag{12}$$

Since magnetic saliency is absent, the reluctance torque component is zero, and the electromagnetic torque depends solely on the q-axis current. This property enables direct torque control through regulation of i_q.

The mechanical dynamics of the generator shaft are governed by:

$$J\frac{d\omega_m}{dt} = T_m - T_e - F\omega_m \tag{13}$$

where J represents the total rotational inertia of the turbine–generator assembly, F is the viscous friction coefficient, and T_m is the mechanical torque supplied by the WT.

The mechanical torque supplied by the WT is derived from the aerodynamic power as:

$$T_m = \frac{P_{\text{aero}}}{\omega_m} \tag{14}$$

In Region-II maximum power operation, where $P_{\text{aero}} = K_{\text{opt}}\omega_m^3$, the mechanical torque becomes:

$$T_m = K_{\text{opt}}\omega_m^2 \tag{15}$$

Substituting (12) and (15) into (13) leads to the coupled nonlinear electromechanical model:

$$J\frac{d\omega_m}{dt} = K_{\text{opt}}\omega_m^2 - \frac{3}{2}p\lambda_m i_q - F\omega_m \tag{16}$$

The rotor position is obtained from:

$$\frac{d\theta_m}{dt} = \omega_m \tag{17}$$

The main parameters of the PMSG used in the simulation model are summarized in Table I.

TABLE I. PARAMETERS OF THE PMSG USED IN THE WT MODEL.

Parameter	Symbol	Value
Stator phase resistance	R_s	0.05 Ω
Synchronous inductance	L_s	1.55 mH
Permanent magnet flux linkage	λ_m	0.98 Wb
Number of pole pairs	p	12
Total inertia	J	0.01993 kg·m^2
Viscous damping coefficient	F	0.0002 N·m·s

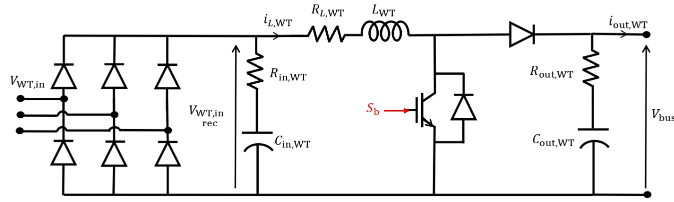

Figure 3. WT AC–DC–DC converter topology.

3) AC–DC–DC Converter: The three-phase output of the PMSG is rectified through a diode bridge and interfaced with the DC–bus using a DC–DC boost converter as shown in Figure 3. Boost converters are commonly used in RE applications to raise the input voltage generated by RESs, particularly when interfacing low-voltage generators such as WTs with a higher-voltage DC–bus. In this study, the DC–bus voltage reference is set to 1000 V, which is a typical design choice in medium-power DC microgrids and industrial DC link systems to ensure compatibility with grid-connected inverters and battery storage systems [19][20].

The three-phase output of the PMSG is first rectified through a diode bridge, producing an unregulated DC voltage that varies with rotor speed. The boost converter then elevates this rectified voltage to the regulated DC–bus level, enabling efficient power transfer under fluctuating wind conditions.

Assuming continuous conduction mode (CCM), the steady-state voltage conversion ratio of the boost converter is given by:

$$\frac{V_{\text{bus}}}{V_{\text{WT, in rec}}} = \frac{1}{1-D} \tag{18}$$

where D is the duty cycle. This relationship shows that the DC–bus voltage can be regulated by adjusting the duty cycle, which is generated by the MPPT-based control loop described in Section III.

The choice of the boost topology is motivated by its simplicity, high efficiency, and reduced component count compared to isolated or multi-stage alternatives [21]. Furthermore, the 10 kHz switching frequency adopted in this study represents a compromise between switching losses and current ripple minimization. The inductance L_{WT} and DC–bus capacitance C_{bus} are selected to ensure stable operation with limited current ripple and acceptable voltage deviation under dynamic wind and load variations.

Assuming negligible mechanical losses and approximates generator efficiency through a constant factor, the electrical power delivered at the rectifier output is expressed as:

$$P_{\text{elec}} = \eta_g\, P_{\text{aero}} \tag{19}$$

where η_g represents the generator efficiency.

The main parameters of the WT boost converter used in the simulation are summarized in Table II.

TABLE II. Parameters of the WT boost converter.

Parameter	Symbol	Value
Input capacitance (rectifier output)	$C_{\mathrm{in,WT}}$	100 μF
Output capacitance (boost output)	$C_{\mathrm{out,WT}}$	500 μF
Input inductance	L_{WT}	1 mH
Inductor resistance	$R_{L,\mathrm{WT}}$	0.01 Ω

B. Battery Energy Storage System

1) Battery Modeling: Due to the intermittent nature of wind energy, the DC microgrid requires an auxiliary energy storage element to ensure power balance and voltage stability. The BESS acts as a dynamic buffer between generation and load, absorbing surplus power during high wind periods and supplying energy when the wind generation is insufficient to meet the thermal demand of the SWHPs.

A lithium-ion BESS is integrated into the DC microgrid to compensate for wind power fluctuations and maintain DC–bus voltage stability. The battery is modeled using the generic lithium-ion model available in Simulink, which captures the nonlinear voltage–State-of-Charge (SOC) characteristics and internal resistance effects.

The battery operates between a fully charged voltage of 407.4 V and a cut-off voltage of 262.5 V. The nominal voltage is 350 V with a rated capacity of 100 Ah, corresponding to an energy storage capacity of 35 kWh.

The main parameters of the BESS used in the simulation are summarized in Table III.

TABLE III. Parameters of the lithium-ion BESS.

Parameter	Symbol	Value
Nominal voltage	V_{nom}	350 V
Rated capacity	Q_{nom}	100 Ah
Internal resistance	R_{int}	0.035 Ω
Fully charged voltage	V_{full}	407.4 V
Cut-off voltage	V_{cut}	262.5 V

2) DC-DC Bidirectional Converter Modeling: To ensure stable operation of the DC–bus, a buck-boost Bidirectional Converter (BDC) is integrated to interface the BESS with the DC microgrid. BDCs are pivotal components for energy management in RE applications, as they enable controlled charge and discharge operation of the battery while regulating the DC–bus voltage. During periods of excess wind generation, the converter operates in buck mode, transferring energy from the DC–bus to the battery. Conversely, when wind generation is insufficient to meet the load demand, the converter operates in boost mode, injecting energy from the battery into the DC–bus. Therefore, their integration is essential for maximizing the utilization of RESs, as they ensure a consistent and reliable power supply.

In the context of HPs, a few studies are found in the literature, including a BESS [22]. The BDC topology adopted in this study is illustrated in Figure 4 [23].

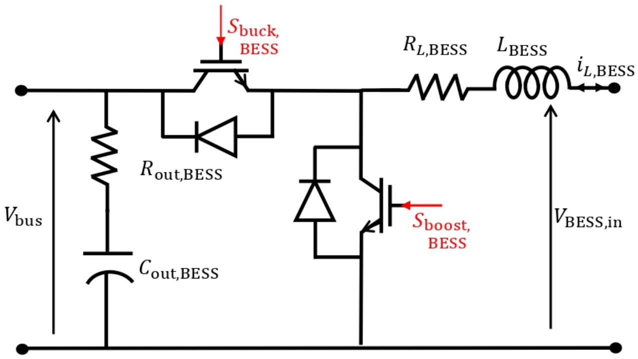

Figure 4. Bidirectional DC–DC converter topology interfacing the BESS.

The main parameters of the BESS BDC used in the simulation are summarized in Table IV.

TABLE IV. Parameters of the BESS BDC converter.

Parameter	Symbol	Value
Output capacitance (boost output)	$C_{\mathrm{out,BESS}}$	500 μF
Input inductance	L_{BESS}	1 mH
Inductor resistance	$R_{L,\mathrm{BESS}}$	0.01 Ω

The equations governing the working principle of the buck and boost modes of this BDC are presented in Eq. (20) [24].

$$\begin{cases} \dfrac{di_{L,\mathrm{BESS}}}{dt} = \dfrac{V_{\mathrm{BESS,in}} - S_{\mathrm{boost,BESS}}\, V_{\mathrm{bus}}}{L_{\mathrm{BESS}}} \\[2ex] \dfrac{dV_{\mathrm{bus}}}{dt} = \dfrac{S_{\mathrm{buck,BESS}}\, i_{L,\mathrm{BESS}} - i_{\mathrm{bus}}}{C_{\mathrm{out,BESS}}} \end{cases} \tag{20}$$

where $i_{L,\mathrm{BESS}}$ denotes the inductor current exchanged with the battery (positive during discharge), V_{bus} is the DC–bus voltage, $S_{\mathrm{boost,BESS}}$ and $S_{\mathrm{buck,BESS}}$ represent the binary switching states of the BDC generated by the control algorithm described in further details in Section III, L_{BESS} and $R_{L,\mathrm{BESS}}$ represent the inductance and its parasitic resistance, respectively, and $C_{\mathrm{out,BESS}}$ is the DC–bus side capacitance associated with the BESS converter.

C. Surface Water Heat Pump

In this model, two identical SWHPs (CIAT DYNACIAT LG 300 A water-to-water HP) are used as parallel loads, providing a nominal heat capacity of 90.3 kW, a cooling capacity of 61.5 kW, and a rated electrical consumption of 29.4 kW.

The primary inputs of the model were the thermal power generated by the SWHPs (Figure 5(a)) and its coefficient of performance (COP) (Figure 5(b)), based on measurements from an installed system at an operational AE harvesting-site in Dijlemolens, Belgium. This site also uses a backup gas boiler to satisfy the total building heat demand. The data covers the period from March 7, 2024 at 11:00 AM to May 7, 2024 at 2:00 AM, with a sample time of five seconds.

The electrical power consumption for the two SWHPs is calculated based on the thermal load profile of the building, as well as the SWHP's technical datasheet. It is given by Eq. (21):

$$P_{\text{e,SWHP}} = \frac{P_{\text{th,SWHP}}}{COP} \tag{21}$$

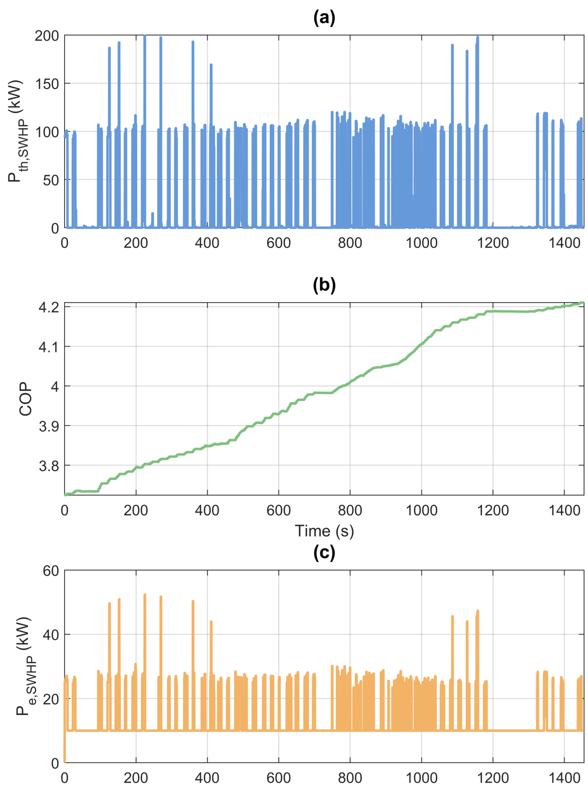

Figure 5. (a) Thermal output power, (b) COP, and (c) electrical consumption of the SWHPs over the simulation period.

As shown in Figure 5, the thermal load profile exhibits frequent peaks in high demand and varying on/off cycles, reflecting realistic building heating demand. Operating in a fully demand-driven mode, these dynamics emphasize the importance of a rapid control response from the supply side and a robust power balance between generation, storage, and load. During periods of low thermal demand, a minimum electrical power of 10 kW is imposed to account for auxiliary electrical equipment and standby operation.

III. Control Strategy of the DC Microgrid

The proposed control framework is designed to regulate the DC–bus voltage, manage bidirectional battery power flow, and ensure safe WT operation across the different operating regions.

A. *Wind Turbine Control Strategy*

1) Region-Based Power Control: Based on the aerodynamic and electromechanical models presented in Section II, the WT control architecture is structured into three hierarchical layers: (i) operating region management and power reference generation, (ii) boost converter current regulation, and (iii) pitch angle control in the above-rated regime [25].

The WT operates in three distinct regions defined by wind speed and rotor speed conditions, as illustrated in Figure 6.

Region-I (Below Cut-in): For wind speeds $v \le 3$ m/s, power production is inhibited, and the reference power is set to zero. This prevents inefficient operation under very low wind conditions.

Region-II (Maximum Power Point Tracking): For wind speeds above cut-in ($V_{\text{cut-in}} = 3$ m/s) and rotor speeds below the rated value $\omega_{\text{rated}} = 21.6$ rad/s (corresponding to the rated wind speed $v_{\text{rated}} = 11.1$ m/s), the turbine operates in maximum power point tracking (MPPT) mode.

In this region, the reference mechanical power $P_{\text{m,ref}}$ follows the optimal torque principle as defined in Eq. (9), ensuring operation at the optimal tip-speed ratio and maximum aerodynamic efficiency. Power regulation is achieved exclusively through generator torque control, while the pitch angle is maintained at $\beta = 0°$ to maximize the aerodynamic power coefficient.

Region-III (Above Rated): When the rotor speed exceeds the rated value $\omega_m > 21.6$ rad/s, the extracted power is limited to the rated turbine power $P_{\text{rated}} = 35$ kW. In this operating regime, the control objective shifts from maximum energy capture to power and speed regulation in order to protect the generator and power electronics.

For wind speeds exceeding the cut-out threshold (20 m/s), the turbine is safely shut down and power production is set to zero to ensure safe operation.

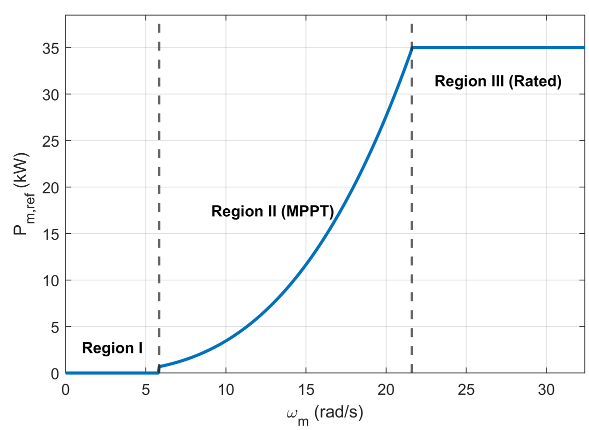

Figure 6. WT operating regions and corresponding power reference as a function of rotor speed.

In Region-III, rotor speed regulation is achieved through blade pitch control. The pitch controller, displayed in Figure 7, is activated when the rotor speed exceeds ω_{rated}, and the speed error is defined as:

$$e_\omega = \omega_m - \omega_{\text{rated}} \tag{22}$$

A proportional–integral (PI) controller generates the pitch β, constrained within the mechanical limits of the turbine:

$$0^\circ \leq \beta \leq 35^\circ \tag{23}$$

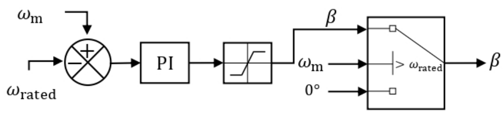

Figure 7. Pitch-based rotor speed regulation.

Increasing the pitch angle reduces the aerodynamic power coefficient $C_p(\lambda, \beta)$, thereby limiting the aerodynamic torque T_m and stabilizing the rotor speed around its rated value. Defining the control error as in Eq. (22) ensures that a positive overspeed condition produces a positive pitch command, enabling effective power limitation in the above-rated region.

2) Boost Converter Current Regulation: The electrical power reference is translated into an inductor current reference for the WT boost converter. Assuming that the mechanical power reference is approximately equal to the electrical power reference (i.e., $P_{\text{m,ref}} \approx P_{\text{elec,ref}}$), the current reference can be obtained from the power–voltage relationship as:

$$i_{L,\text{WT,ref}} = \frac{P_{\text{elec,ref}}}{V_{\text{WT,in rec}}} \tag{24}$$

As shown in Figure 8, an inner current control loop regulates the measured inductor current i_L using a PI controller. The control error is defined as:

$$e_i = i_{L,\text{WT,ref}} - i_{L,\text{WT}} \tag{25}$$

The PI controller generates the duty cycle of the boost converter, ensuring fast dynamic tracking of the reference power. Current saturation and voltage-based enabling mechanisms are included to guarantee safe converter operation under transient conditions.

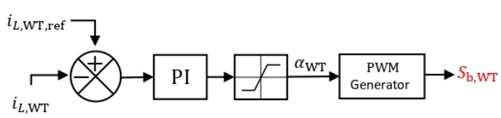

Figure 8. Inductor current control loop of the WT boost converter.

B. BESS Control Strategy

The control of the battery-side BDC is based on maintaining the DC–bus voltage at its nominal value of 1000 V while managing the direction of power flow (buck or boost mode) according to the instantaneous power balance between the renewable source and the load. To achieve this objective, a cascaded dual-loop control structure is implemented, combining DC–bus voltage regulation with bidirectional current control.

An outer voltage control loop regulates the measured DC–bus voltage V_{bus} around its reference value $V_{\text{bus,ref}}$. The corresponding voltage error is defined as:

$$e_v = V_{\text{bus,ref}} - V_{\text{bus}} \tag{26}$$

A PI controller processes this error and generates the reference battery current $i_{\text{BESS,ref}}$, which determines whether the battery should charge or discharge.

An inner current control loop then regulates the measured inductor current $i_{\text{BESS,in}}$ according to:

$$e_i = i_{L,\text{BESS,ref}} - i_{L,\text{BESS}} \tag{27}$$

The current PI controller produces the duty cycle command α_{BESS}, which is forwarded to the converter mode management logic. The complete control architecture is illustrated in Figure 9.

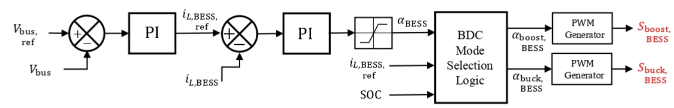

Figure 9. PWM control signals for buck and boost switches for the BESS BDC.

The bidirectional operating mode is selected based on the sign of $i_{L,\text{BESS,ref}}$ and the battery state of charge $\text{SOC}(t)$, as detailed in the flowchart of Figure 10. When $i_{L,\text{BESS,ref}} \geq 0$ and $\text{SOC}(t) > \text{SOC}_{\text{min}}$, the converter operates in boost mode (battery discharging). In this case, the corresponding duty cycles are assigned as:

$$\alpha_{\text{boost,BESS}} = \alpha_{\text{BESS}}, \qquad \alpha_{\text{buck,BESS}} = 0 \tag{28}$$

Conversely, when $i_{L,\text{BESS,ref}} < 0$ and $\text{SOC}(t) < \text{SOC}_{\text{max}}$, the converter operates in buck mode (battery charging), with:

$$\alpha_{\text{boost,BESS}} = 0, \qquad \alpha_{\text{buck,BESS}} = 1 - \alpha_{\text{BESS}} \tag{29}$$

If neither condition is satisfied, both duty cycles are set to zero to prevent operation outside the allowable SOC limits.

This hierarchical control structure ensures stable DC–bus voltage regulation, proper bidirectional power flow, and safe battery operation within predefined SOC constraints, limited to 20% and 80% for SOC_{min} and SOC_{max}, respectively, to preserve battery lifetime and operational safety.

IV. RESULTS | DISCUSSION

The system configuration previously defined in Figure 1 is simulated in MATLAB/Simulink to validate the architecture under realistic operating conditions.

Figure 11 illustrates the evolution of the blade pitch angle β and the aerodynamic power coefficient C_p over the entire simulation period (1456 s). During Region-II operation (below rated wind conditions), the pitch angle remains at $\beta = 0^\circ$, and the power coefficient stabilizes around its optimal value $C_{p,\text{max}} \approx 0.53$, confirming proper MPPT behavior. In this regime, power regulation is achieved solely through generator torque control without aerodynamic intervention.

When the wind speed exceeds its rated value ($v_{\text{rated}} = 11.1$ m/s), corresponding to a rotor speed threshold of $\omega_{\text{rated}} = 21.6$ rad/s, the pitch controller is activated. The pitch angle increases progressively, reaching values up to approximately

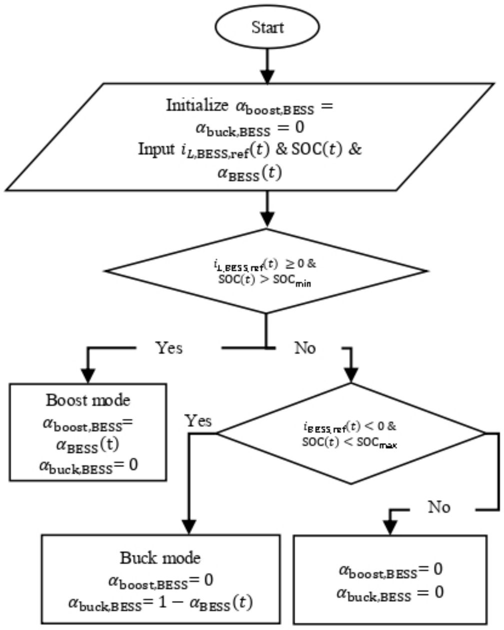

Figure 10. Flowchart of the BDC mode selection logic for the BESS.

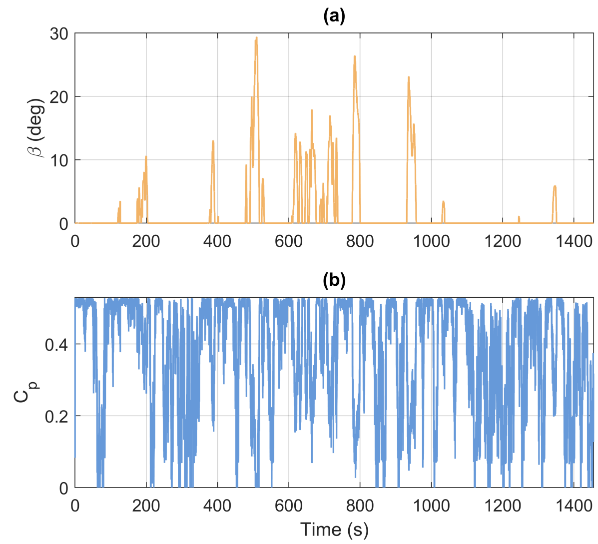

Figure 11. Evolution of (a) blade pitch angle β and (b) aerodynamic power coefficient C_p during WT operation over the simulation period.

$29.37°$ during high wind events. As a consequence, the aerodynamic power coefficient decreases from its optimal value to below $C_p \approx 0.35$, effectively reducing the aerodynamic torque and limiting the mechanical power transferred to the generator.

Under extreme wind conditions, the effectiveness of the pitch-based regulation and the cut-out protection mechanism is clearly demonstrated. At the maximum recorded wind speed of 20.83 m/s (at $t = 509$ s), the pitch controller is strongly activated, with the blade angle reaching values close to its upper operating range (up to $\beta = 29.37°$). As a result, the aerodynamic power coefficient decreases significantly, dropping to $C_p = 0.0414$ and approaching zero during peak pitch activation. This reduction in C_p confirms that the WT is effectively de-loaded aerodynamically under high wind conditions, substantially limiting the extracted mechanical power.

Moreover, once the wind speed exceeds the cut-out threshold of 20 m/s, the electrical reference power is automatically forced to zero ($P_{\text{e,ref}} = 0$ W), validating the correct activation of the shutdown logic. This two-stage protection mechanism—progressive aerodynamic de-loading through pitch regulation followed by complete shutdown above cut-out—ensures safe WT operation while preventing excessive energy conversion and generator overloading in severe wind events.

Figure 12 presents the closed-loop tracking performance of the WT current loop, the BESS current loop, and the DC–bus voltage over the entire simulation horizon.

For the WT inductor current, the peak value reaches 91.6 A while the root-mean-square (RMSE) tracking error remains limited to 6.04 A, corresponding to approximately 6.6% of the peak current. The larger instantaneous deviations occur during rapid power transitions, whereas steady-state tracking remains accurate and well damped.

The BESS current loop exhibits stable bidirectional regulation during both charging and discharging phases. The peak current reaches 138.16 A, with a maximum instantaneous error of 53.59 A. The RMSE is 7.85 A (approximately 5.7% of the peak value), indicating consistent current control despite dynamic power exchange within the microgrid.

At the system level, the DC–bus voltage is tightly regulated around the nominal 1000 V. The voltage varies between 993.78 V and 1003.47 V, yielding a peak-to-peak deviation of 9.70 V (0.97%). The maximum absolute voltage deviation from its reference remains below 0.62%, while the RMS voltage error is only 0.332 V, corresponding to 0.033% of nominal voltage, demonstrating robust voltage stability under fluctuating wind input and high thermal demand.

The SOC trajectory, displayed in Figure 13, remains well within the predefined operational limits of 20% and 80% throughout the simulation period. The SOC varies between 69.06% and 71.55%, with an average value of 70.23%, corresponding to a total swing of approximately 2.5%. This limited variation indicates that the wind generation and load demand remain largely balanced over the studied period, while the BESS effectively compensates short-term power mismatches. Moreover, the absence of boundary saturation confirms that the proposed energy management strategy successfully prevents deep discharge and overcharge conditions, thereby ensuring safe battery operation and enhanced lifetime.

Figure 14 presents the instantaneous power exchange at the DC–bus between the WT, BESS, and the two SWHPs. The BESS power is considered positive when discharging to the DC–bus and negative during charging.

The BESS operates fully bidirectionally, with a maximum discharge power of 51.38 kW and a maximum charging

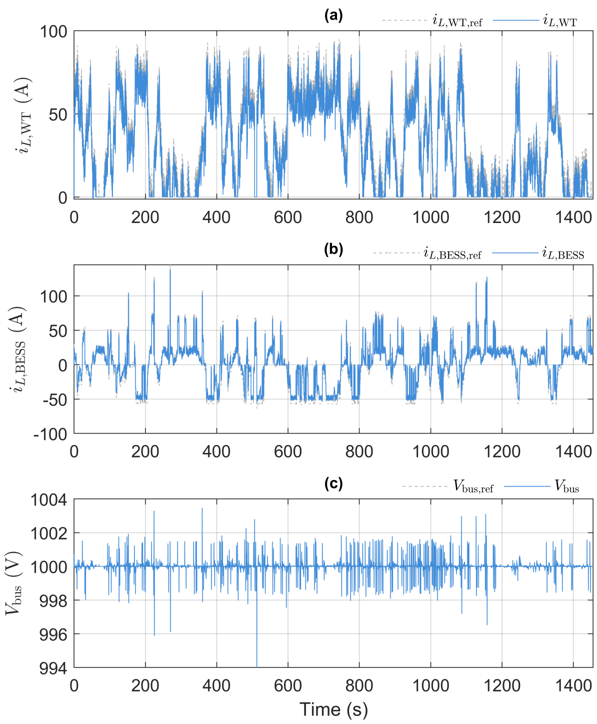

Figure 12. Closed-loop control performance: (a) $i_{L,\mathrm{WT}}$ tracking, (b) $i_{L,\mathrm{BESS}}$ tracking, and (c) V_{bus} regulation.

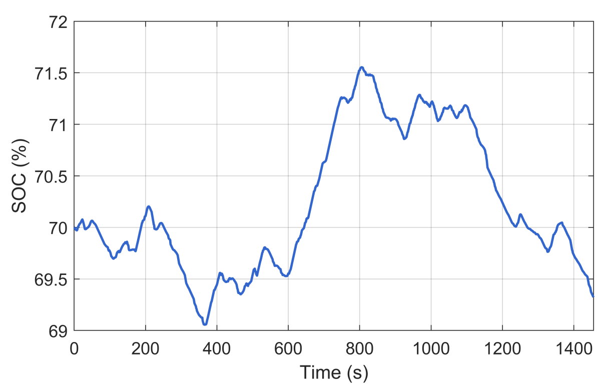

Figure 13. SOC evolution of the BESS over the simulation period.

power of 21.29 kW. The converter remains in discharge mode during 50.55% of the simulation time and in charge mode during 49.45%, indicating balanced alternating power buffering behavior driven by wind-load mismatch dynamics.

The instantaneous DC–bus power balance was evaluated as

$$P_{\mathrm{WT}} + P_{\mathrm{BESS}} - P_{\mathrm{SWHPs}}$$

The mean absolute power imbalance remains limited to 2.46 kW (approximately 4.7% of the peak load), confirming that short-term mismatches are effectively absorbed by the DC–bus capacitor without compromising system stability. This result is consistent with the previously observed voltage deviation below 1%, demonstrating dynamic consistency of the model.

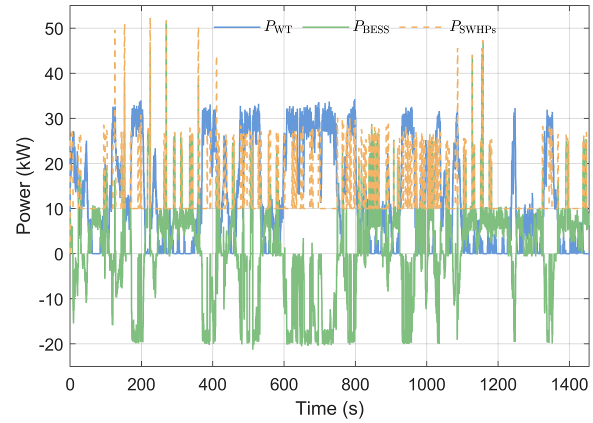

Figure 14. DC–bus power balance between the WT, BESS, and SWHPs over the simulation period.

A critical operating condition occurs at $t = 225$ s, where the SWHPs demand reaches its maximum value of 52.32 kW. At this instant, the WT supplies only 6.33 kW, while the BESS delivers 42.80 kW to the DC–bus. The combined generation therefore reaches 49.13 kW, resulting in a transient deficit of 3.19 kW (approximately 6.1% of the peak load). This mismatch is temporarily compensated by the DC–bus capacitance, confirming the robustness of the coordinated control strategy.

A complementary operating condition occurs at $t = 512.40$ s, corresponding to the maximum battery charging event. At this instant, the WT produces 29.85 kW while the load demand is only 10.00 kW, resulting in a surplus of 19.85 kW. The BESS absorbs 21.29 kW, thereby preventing renewable curtailment and maintaining DC–bus stability. The instantaneous residual is limited to 1.44 kW (approximately 4.8% of the WT power), confirming effective transient buffering by the DC–bus capacitance. This event validates the proper activation of the buck operating mode and demonstrates the ability of the BESS to capture excess wind energy under low-demand conditions.

The selected BESS capacity therefore provides sufficient power support during peak demand events while maintaining operation within a narrow SOC range, thereby preserving battery lifetime and preventing deep charge/discharge cycling. The limited SOC variation observed during the simulation confirms that the system operates in a dynamic buffering regime, where the BESS primarily compensates short-term power imbalances rather than serving as long-term energy storage.

Overall, the results demonstrate that the proposed WT–BESS architecture ensures stable dynamic power sharing, enforces rated WT power limitation, and maintains supply continuity under both wind deficit and high-demand conditions. Thus, the proposed configuration enables simulated fully RE-powered operation under the studied operating conditions, without reliance on auxiliary fossil-fuel backup.

V. Conclusion and Future Work

This paper presented the design and validation of a DC-coupled hybrid WT–BESS–SWHP microgrid based on realistic climatic data from Le Cano Ouistreham, France pilot site and thermal demand data from an operational aquathermal installation in Dijlemolens, Belgium. A coordinated hierarchical control strategy combining Region-II MPPT, refined Region-III pitch regulation, and cascaded voltage–current control loops was implemented to ensure stable demand-driven operation under fluctuating wind conditions.

Simulation results demonstrate robust system performance under dynamic operating scenarios. The DC–bus voltage remained tightly regulated around its nominal value of 1000 V, with a maximum deviation limited to 0.62%, and an RMSE of only 0.033%. During the most critical operating condition, corresponding to a peak thermal demand of 52.32 kW, coordinated power sharing between the 35 kW WT and the 35 kWh BESS ensured supply continuity without violating operational constraints. The BESS delivered up to 51.38 kW during discharge events while maintaining the SOC within a narrow 2.5% swing (69.06%–71.55%), confirming effective short-term buffering and safe operation.

The results validate the proposed DC microgrid architecture as a realistic and scalable framework for renewable-powered aquathermal heating systems. Future work will focus on the investigation of advanced DC–DC converter topologies, along with corresponding advanced control strategies, to further improve dynamic response, power quality, and overall system efficiency of the proposed DC microgrid.

Acknowledgment

This work was carried out at the GREAH laboratory, University of Le Havre Normandie, particularly by the "Renewable Energies and Storage Systems" (MERS) team, within the framework of the Interreg WaterWarmth project, co-funded by the European Union. The authors would like to thank the European Union and the University of Le Havre Normandie for their financial support.

References

[1] J. Assaf, M.-B. Camara, D. Guilbert, and B. Dakyo, “Energy management of a wind–battery powered surface water heat pump system”, in *Proceedings of the Tenth International Conference on Green Communications, Computing and Technologies (GREEN 2025)*, Barcelona, Spain: IARIA, Oct. 2025, pp. 16–21, ISBN: 978-1-68558-311-8.

[2] J. D. Spitler and M. S. Mitchell, “Surface Water Heat Pump Systems”, in *Advances in Ground-Source Heat Pump Systems*, Elsevier, 2016, pp. 225–246.

[3] E. Brasser, “Heating Houses Using Surface Water: A Sustainable Alternative to Natural Gas”, Ph.D. dissertation, Delft University of Technology, Delft, Netherlands, 2020.

[4] International Renewable Energy Agency (IRENA), “Regional Energy Transition Outlook: European Union”, IRENA, Abu Dhabi, Report, 2025.

[5] A. Żelazna and A. Pawłowski, “Review of the Role of Heat Pumps in Decarbonization of the Building Sector”, *Energies*, vol. 18, no. 13, 2025, ISSN: 1996-1073. DOI: 10.3390/en18133255.

[6] Eurostat, “Electricity from renewable sources reaches 47% in 2024”, 2025, Accessed: May 6, 2026. [Online]. Available: https://ec.europa.eu/eurostat/web/products-eurostat-news/w/ddn-20250319-1.

[7] D. Rekioua, “Hybrid Renewable Energy Systems Overview”, in *Hybrid Renewable Energy Systems: Optimization and Power Management Control*, Springer, 2019, pp. 1–37.

[8] N. Bayati, A. Hajizadeh, and M. Soltani, “Protection in DC Microgrids: A Comparative Review”, *IET Smart Grid*, vol. 1, no. 3, pp. 66–75, 2018. DOI: 10.1049/iet-stg.2018.0024.

[9] S. Baraskar, D. Günther, J. Wapler, and M. Lämmle, “Analysis of the Performance and Operation of a Photovoltaic-Battery Heat Pump System Based on Field Measurement Data”, *Solar Energy Advances*, vol. 4, p. 100 047, 2024. DOI: 10.1016/j.seadv.2023.100047.

[10] A. V. Klokov, A. S. Tutunin, E. S. Sharaborova, A. A. Korshunov, and E. Y. Loktionov, “Inverter Heat Pumps as a Variable Load for Off-Grid Solar-Powered Systems”, *Energies*, vol. 16, no. 16, p. 5987, 2023, ISSN: 1996-1073. DOI: 10.3390/en16165987.

[11] M. Bojić, N. Nikolić, D. Nikolić, J. Skerlić, and I. Miletić, “Toward a Positive-Net-Energy Residential Building in Serbian Conditions”, *Applied Energy*, vol. 88, no. 7, pp. 2407–2419, 2011, ISSN: 0306-2619. DOI: 10.1016/j.apenergy.2011.01.015.

[12] C. Roselli, M. Sasso, and F. Tariello, “Dynamic Simulation of a Solar Electric Driven Heat Pump for an Office Building Located in Southern Italy”, *International Journal of Heat and Technology*, vol. 34, no. S2, S496–S504, 2016, ISSN: 0392-8764. DOI: 10.18280/ijht.34S243.

[13] L. Yang, N. Tai, C. Fan, and Y. Meng, “Energy Regulating and Fluctuation Stabilizing by Air Source Heat Pump and Battery Energy Storage System in Microgrid”, *Renewable Energy*, vol. 95, pp. 202–212, 2016, ISSN: 0960-1481. DOI: 10.1016/j.renene.2016.04.026.

[14] C. B. N. Fapi, M. L. Touré, M.-B. Camara, and B. Dakyo, “Control Strategy for DC Micro-Grids in Heat Pump Applications with Renewable Integration”, *Electronics*, vol. 14, no. 1, p. 150, 2025, ISSN: 2079-9292. DOI: 10.3390/electronics14010150.

[15] C. B. N. Fapi, M. L. Touré, M.-B. Camara, and B. Dakyo, “MPPT Based Fractional Short-Circuit Current-Model Predictive Control for PV System in Real Weather Conditions for Heat-Pump Applications”, in *Proceedings of the 2024 International Conference on Intelligent Systems and Computer Vision (ISCV 2024)*, IEEE, 2024, pp. 1–6. DOI: 10.1109/ISCV61718.2024.10694395.

[16] C. B. N. Fapi, M. L. Touré, M.-B. Camara, and B. Dakyo, “High Voltage Gain DC-DC Converter Based Maximum Power Tracking from Photovoltaic Systems for Heat-Pump Applications”, in *Proceedings of the 2024 12th International Conference on Smart Grid (icSmartGrid 2024)*, IEEE, 2024, pp. 493–498. DOI: 10.1109/icSmartGrid61521.2024.10557289.

[17] B. Singh and S. Sharma, “Stand-alone wind energy conversion system with an asynchronous generator”, *Journal of Power Electronics*, vol. 10, no. 5, pp. 538–547, 2010, ISSN: 1598-2092.

[18] E. Chavero-Navarrete, M. Trejo-Perea, J.-C. Jáuregui-Correa, R.-V. Carrillo-Serrano, and J.-G. Rios-Moreno, “Pitch angle optimization by intelligent adjusting the gains of a PI controller for small wind turbines in areas with drastic wind speed changes”, *Sustainability*, vol. 11, no. 23, p. 6670, 2019, ISSN: 2071-1050. DOI: 10.3390/su11236670.

[19] K. B. Samal, S. Pati, and R. Sharma, “Power Management Using an Improved EMS Algorithm in a Stand-Alone Hybrid PV-PEMFC Microgrid with Reduced Converter Count”, *Green Energy and Intelligent Transportation*, p. 100 302, 2025, ISSN: 2772-3755. DOI: 10.1016/j.get.2025.100302.

[20] K. Zafar, M. K. Kamaludeen, Y. Esa, A. A. A. Mohamed, and S. Odie, “Fault Analysis for DC Bus-Integrated Energy

Storage System, Electric Vehicle Supply Equipment, and Photovoltaic Systems", *Electric Power Systems Research*, vol. 234, p. 110 837, 2024, ISSN: 0378-7796. DOI: 10.1016/j.epsr.2024.110837.

[21] J. Assaf, J. S. Menye, M. B. Camara, D. Guilbert, and B. Dakyo, "Power Converter Topologies for Heat Pumps Powered by Renewable Energy Sources: A Literature Review", *Electronics*, vol. 13, no. 19, p. 3965, 2024, ISSN: 2079-9292. DOI: 10.3390/electronics13193965.

[22] C. Lorenzo, L. Narvarte, R. H. Almeida, and A. B. Cristóbal, "Technical Evaluation of a Stand-Alone Photovoltaic Heat Pump System Without Batteries for Cooling Applications", *Solar Energy*, vol. 206, pp. 92–105, 2020, ISSN: 0038-092X. DOI: 10.1016/j.solener.2020.05.051.

[23] M. B. Camara, "Supercapacitors for Dynamic Energy Exchange Onboard Hybrid Electric Vehicles: Modeling, Converter Study, and Control", Ph.D. dissertation, Université de Franche-Comté, France, 2007.

[24] S. Agrawal, L. Umanand, and B. S. Reddy, "Bidirectional Current-Fed Converter for High Gain DC–DC and DC–AC Applications", in *Proc. of the Symposium on Power Electronic and Renewable Energy Systems Control (PERESC 2020)*, ser. Lecture Notes in Electrical Engineering, vol. 731, Singapore: Springer, 2021, pp. 101–111. DOI: 10.1007/978-981-33-4081-9_10.

[25] D. Ikni, M. B. Camara, A. Payman, and B. Dakyo, "Dynamic control of wind energy conversion system", in *Proceedings of the 8th International Conference and Exhibition on Ecological Vehicles and Renewable Energies (EVER 2013)*, IEEE, 2013, pp. 1–5. DOI: 10.1109/EVER.2013.6521561.